High-Frequency Modeling of Electrical Drive Systems Considering Test Bench Environment Influence

Hujun Peng, Yue Yu, Svetomir Stevic, *Graduate Student Member, IEEE*, and Simon Steentjes

***Abstract*—This study addresses the challenges of high-frequency modeling in electrical drive systems, particularly considering the influence of the test bench environment. A universal grey-box modeling approach is developed to accurately represent the frequency-dependent behaviors of permanent magnet synchronous machines (PMSMs) and cable sets up to 10 MHz. The proposed method integrates impedance measurements and parameterization to model complex effects such as the skin effect, proximity effect, and parasitic capacitance. The influence of the test bench environment, particularly on the cable set's layout and electromagnetic interference from the test bench, is systematically analyzed and incorporated into the model. Validation results in both frequency and time domains demonstrate a significant improvement in model accuracy. This work provides a robust framework for high-frequency modeling, enhancing the design and optimization of insulation systems and the prediction of transient behaviors in electric drives.**

***Index Terms*—Grey box model, high-frequency modeling, permanent magnet synchronous machine (PMSM), test bench, transient overvoltage.**

I. INTRODUCTION

PERMANENT-MAGNET synchronous machines (PMSMs) are extensively utilized in the automotive industry due to their compact size, lightweight design, high power density, and excellent mechanical characteristics [1], [2], particularly in high-speed and high-torque applications [3]. The integration of power modules using Wide-Bandgap Semiconductors (WBGs), such as SiC and GaN-based MOSFETS with high switching frequencies and slew rates [4], is increasingly adopted in practice because of their superior performance in reducing torque and speed ripple and minimizing power losses under various operating conditions compared to IGBT devices [5]. However, the high voltage slew rates of WBGs introduce increased overvoltage oscillations during switching transitions at motor terminals and along windings [6], [7]. In cases of double-pulsing effects, the peak voltage can reach up to four times the dc-link voltage [8], presenting significant challenges for motor insulation systems to comply with IEC 60034-18-41 standards [9]. A common countermeasure is overdesigning machine insulation systems [10], which can be optimized by accurately predicting maximum voltage stress between windings and housing using high-frequency modeling.

High-frequency models are generally classified as white-box or gray-box models. The white-box model connects the equivalent electrical circuit of each conductor into a complete electrical network based on the winding scheme [11], [12]. The model is parameterized by using finite-element analysis (FEA) based on geometric constructions and material parameters. However, the high computational demand often limits its application. Moreover, the frequency-dependent permeability of materials at frequencies up to several megahertz [13] is often not available because the labor measurement of soft magnetic materials is restricted to several tens of kilohertz, which is far lower than required for high-frequency modeling.

In contrast, the gray-box model is typically employed for existing electric machines and focuses on analyzing frequency-dependent interactions within the machines from an external perspective. The parameterization process relies on impedance measurements and curve-fitting algorithms [14]. For instance, a three-phase gray-box model of an induction machine is proposed in [15], based on common-mode (CM) and differential-mode (DM) impedance measurement at the machine terminals. However, the CM and DM models have not been integrated into one model, and there is insufficient description of the frequency-dependent proximity effect in the high-frequency range. Before we research high-frequency modeling of electrical machines, the state-of-the-art technique is limited to modeling the skin effect using a resistor-inductor-ladder network and the proximity effect using current-controlled voltage sources for the inductive coupling aspect or a simple mutual inductance structure without considering the frequency dependency. Sundeep et al. [16] used the current-controlled voltage sources to assess the proximity effect. However, one of the most significant drawbacks is that the coupling between every two windings is separately considered, which hugely increases the number of parameters needed to describe the entire inductive coupling network between all different phases and windings. More importantly, there is no relation between the parameters of one coupling network and another, which is, in reality, not accurate because all the windings in inductive coupling share the common main inductive path

Received 12 December 2024; revised 28 March 2025; accepted 24 April 2025. Date of publication 2 May 2025; date of current version 30 June 2025. Recommended for publication by Associate Editor C. K. Tse. *(Corresponding author: Hujun Peng.)*

Hujun Peng, Yue Yu, and Simon Steentjes are with the Institute of Electrical Machines, RWTH Aachen University, 52062 Aachen, Germany (e-mail: hujun.peng@iem.rwth-aachen.de).

Svetomir Stevic is with Schabmüller GmbH, 92334 Berching, Germany.

Color versions of one or more figures in this article are available at https://doi.org/10.1109/TPEL.2025.3566700.

Digital Object Identifier 10.1109/TPEL.2025.3566700

and lie in a similar position and environment. Therefore, the representative work introduces a structure for considering the frequency-dependent proximity effect, which, however, has a vast parameter tuning expense and does not fully consider the physical constraint to the model parameters. In order to solve the limitation in modeling the frequency-dependent proximity effect regarding universality and easiness of use, a resistor-mutual inductor-ladder network to consider the frequency dependency of the proximity effect between different windings in our previous studies [17], [18], [19], [20], [21]. Thereby, in [17] and [22], a coil-based gray-box model is developed for a PMSM with a hairpin stator winding, while the model in [18] focuses on the single-tooth winding of a PMSM stator. Then, Peng et al. [20] introduced a conductor-level grey-box model for the hairpin stator winding of a PMSM. These models incorporate detailed considerations of frequency-dependent effects based on the winding configuration schema. Furthermore, a general model structure applicable to three-phase systems is proposed in [19] and [21] to model the transient overvoltage at machine terminals for various electrical machines. Although high accuracy in the previously developed models for high-frequency grey box modeling of electrical machines, the proposed structure did not differentiate between skin and proximity effects because, in the layer structure, some layers have inductance while some layers have mutual inductance. Therefore, the proposed structure is not convenient for readers to use; in other words, it is not general enough. Therefore, this contribution aims to develop a more universal and easily accessible structure compared to previous models presented in [19], [21]. Although the skin and proximity effects exhibit similar characteristics during measurements, their distinct underlying causes necessitate modeling approaches differentiating these two phenomena.

Furthermore, for accurate modeling of transient overvoltages within the entire drive system, the high-frequency behavior of power cables must be accurately considered [23]. Notably, with the introduction of WBG, there remains a significant risk of insulation layer degradation and unexpected winding insulation failures, even when the length of the power cables is reduced to one-tenth of that used in conventional designs based on traditional IGBTs [24]. Xu et al.[8] highlighted the high-frequency behavior of cables with the introduction of WBG devices. However, no universally reliable high-frequency cable model has been established. In [25], a 150-m-long three-conductor shielded power cable is modeled using a multiport linear network, which does not represent the typical application scenario of PMSMs in the automotive industry. In [16], a high-frequency model for a 2.5-m-long shielded cable is developed, but the inductive coupling between different phases is not considered. Overall, the high-frequency cable models, whose state-of-the-art is similar to those machine models found in the literature, have identical drawbacks in considering the frequency-dependent proximity effect. One representative work on cable modeling in [26] considers the mutual inductance among phase conductors and shields. However, there is no ladder structure like the one we introduce later, and the dependence of the proximity effect on the frequency is not considered. It merely finds the frequency-dependent skin effect using a 2-layer ladder network structure. Therefore, this contribution aims to develop a more general cable model than the state-of-the-art in [26].

Moreover, previous studies have not validated the existence of electrical machines and cables on real test benches. For modeling electrical machines, the literature validates high-frequency machine models using a stator with coils instead of a real running rotor [16], [27]. For validating power cable models found in the literature, large insulation layers such as paper boxes and gummy layers are used instead of an actual test bench with metallic materials. By using the insulation layers, the influence of the metallic test bench on the cables is excluded, which makes validation significantly easier. However, the real test bench and application scenarios with a metallic surface can introduce further previously unknown disturbances. Validating high-frequency models on a test bench requires considering the influence of test benches made of metallic materials. The reason is that the power cables are directly laid on the metallic surface of test benches, which inevitably causes capacitive and inductive coupling between cables and test benches. Therefore, another goal of this contribution is to enable model validation on real application scenarios while considering the influence of the test bench and environment.

In order to address the gap in the grey-box modeling of the electrical drive systems mentioned, the following contributions are summarized.

1) A universal grey-box model for electrical machines is proposed, with a novel structure for differentiating skin and proximity effects.
2) A universal model for shielded cable sets is created, capturing frequency-dependent proximity effect up to 10 MHz.
3) The impact of the test bench environment on the electrical drive system's frequency-response properties is identified and evaluated.
4) The model parameters of the electrical drive system are adjusted based on the test environment and validated in the frequency domain to consider the environmental influence.
5) The model is validated in the time domain using measurements from a test bench with a running electrical machine at different operation conditions. This validation underscores the significant influence of considering the test bench environment in the high-frequency models of the entire drive system. The deviation between modeled and measured signals is reduced from over 100 % using the model without considering test bench influence to less than 10 % using adjusted models on average regarding peak values and oscillation frequency during switching processes.

The rest of this article is organized as follows: Section II introduces grey-box modeling based on impedance measurements for each component. Section III analyzes the impact of the test environment on high-frequency behavior. Section IV proposes model adjustment methods and validates the complete model in the time domain by comparing simulation results with test measurements, highlighting the impact of the testbench environment on high-frequency modeling. Finally, Section V concludes this article.

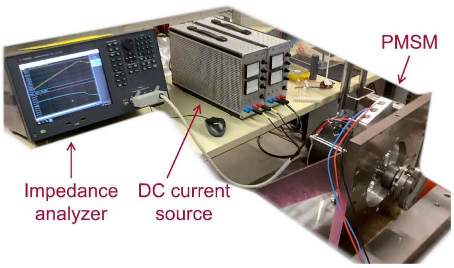

Fig. 1. Setup for PMSM impedance measurement includes an impedance analyzer, a DC current source, and the PMSM being measured.

TABLE I
CONNECTION TERMINAL TOPOLOGIES FOR MEASURING IMPEDANCE SPECTRA OF THE PMSM

Category	Example	Impedance between one phase terminal and
phase-to-housing	U-GND	machine housing
phase-to-phase	U-V	another phase-terminal
phase-to-phases	U-VW	the other shorted phases

II. GREY-BOX MODELING APPROACH

The high-frequency behavior of windings and cable sets exhibits nonlinear responses influenced by frequency-dependent effects, including the skin effect, proximity effect, parasitic capacitance, and wave propagation and reflection phenomena. To address these effects, grey-box models are developed based on measured impedance spectra of components up to 10 MHz in the frequency domain, enabling the characterization of frequency-dependent behaviors through lumped parameter representations in the time domain. The following section provides a detailed description of the grey-box models developed for both the electrical machines and the cable set.

A. Development of the PMSM Model

1) Impedance Measurement: The PMSM used in this study has single-tooth winding with 8 pole pairs and 24 slots. Each of the U, V, and W phases consists of four parallel branches, with each branch comprising two coils connected in series, forming a total of four neutral points. The amplitude and phase profiles of terminal impedance were measured across frequencies ranging from 100 Hz to 10 MHz using the Keysight E4990 A impedance analyzer, as illustrated in Fig. 1. The measurements were performed under different terminal connection configurations, categorized into three main categories: phase-to-housing, phase-to-phase, and phase-to-two-phases, as summarized in Table I. In these illustrations, "UV" for example, indicates a short-circuit connection between terminals U and V, while "GND" signifies a connection to the housing. A dc current source was used to adjust the rotor position prior to measurement, ensuring consistency. Previous studies have indicated that the influence of rotor position can be neglected in high-frequency modeling of stator winding [28]. Therefore, measurements and modeling were conducted at a single standardized rotor position.

Fig. 2 presented the results of PMSM impedance measurement. Impedance spectra within the same category exhibit consistent patterns. Observing the frequency range below 200 kHz, the PMSM demonstrates the capacitive properties of its insulation system, with the phase angle of CM-impedance (phase-to-housing) remaining at -90°. Meanwhile, the DM-impedance (phase-to-phase and phase-to-phases) exhibit inductive behavior, with their phase angles maintaining $+90^\circ$. Above the 100 kHz threshold, the influence of parasitic capacitance between the winding and the machine housing becomes dominant, resulting in an increase in both amplitude and phase with rising frequency, up to the first resonance point at approximately 1 MHz. As the frequency increases further, the DM-impedance gradually approaches -90°, a phenomenon attributed to the effects of parasitic capacitance along the winding and other internal cross-coupling interactions. The properties exhibited in measured spectra should be recommended for consideration during modeling.

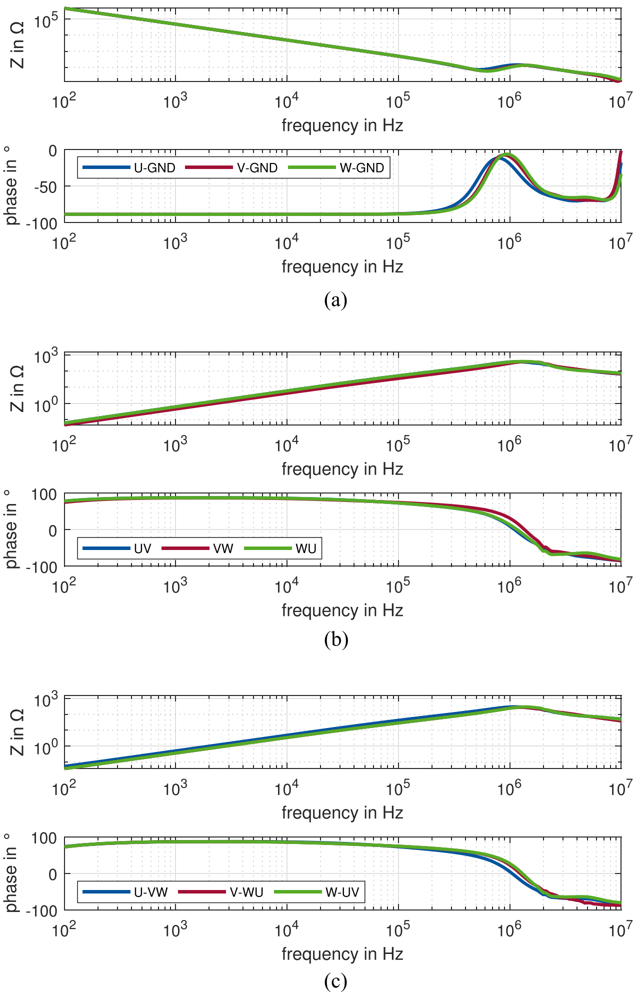

Fig. 2. Impedance measurement results of the PMSM stator winding. (a) Phase-to-housing. (b) Phase-to-phase. (c) Phase-to-phases.

2) Grey-Box Model Implementation: Fig. 3(a) illustrates the structural overview of the grey-box model for the PMSM stator winding. Based on the properties and spectral profiles obtained from impedance measurements, a modular model with two branches is designed to encompass all major resonance points. In this model, the machine housing is considered as the zero-potential reference. The components and subsystems in

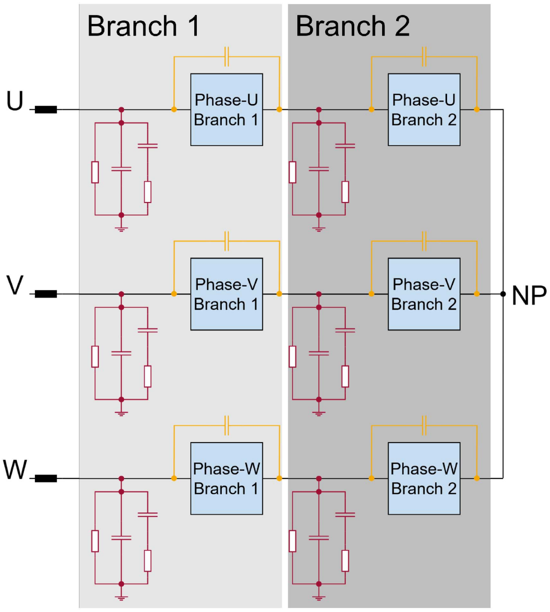

(a)

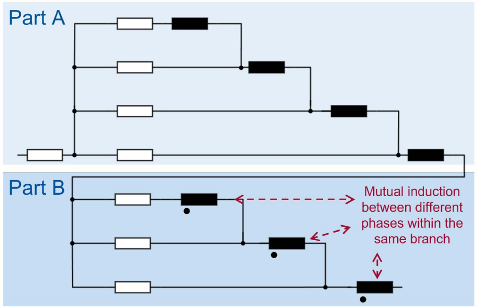

(b)

Fig. 3. Grey-box model of the PMSM stator windings. (a) Structural overview. (b) Conductor model details with mutual inductance.

Fig. 3(b), marked in different colors, simulate various frequency-dependent phenomena.

Essentially, the winding of each phase is modeled as an independent part, highlighted by blue blocks in Fig. 3(a), which is characterized by an impedance phase angle approaching $+90^\circ$ under ac excitation and an increasing resistance due to the skin effect. At high frequencies, the skin effect causes current to concentrate near the surface of the conductor, effectively increasing its resistance and reducing the cross-sectional area available for current flow. The penetration depth of the current is given by

$$\delta = \sqrt{\frac{2\rho}{\omega \cdot \mu}} \tag{1}$$

where ρ is the resistivity, μ is the permeability, and ω is the angular frequency. The resistor–inductor–ladder network (RL-ladder-network) is commonly used to model this effect because it effectively represents the distributed nature of eddy currents in the conductor. By discretizing the conductor cross-section into layers, where each layer has an associated series resistance (to capture the increased resistance at higher frequencies) and inductance (to model the self-inductance of current flowing in different layers), the RL ladder network mimics the gradual reduction of current penetration at increasing frequencies. In prior literature, RL ladder networks have been successfully used to model high-frequency behavior in power cables, transformer windings, and electromagnetic shielding structures. The approach is computationally efficient compared to full finite-element simulations while maintaining high accuracy in capturing the frequency-dependent resistance behavior.

However, the proximity effect cannot be neglected due to the tightly packed three-phase windings within the machine. The proximity effect arises due to mutual inductance between adjacent conductors, leading to nonuniform current distribution and further increasing ac resistance. Unlike the skin effect, which is a self-effect within a conductor, the proximity effect is an interaction between conductors and highly depends on their relative spacing and frequency. We introduce a resistor-mutual inductor-ladder network to model the frequency-dependent proximity effect (RM-ladder-network). This network extends the RL ladder by incorporating mutual inductances between conductor layers. The additional mutual inductive coupling elements capture the redistribution of current caused by external magnetic fields, which is not accounted for in a simple RL ladder network.

In order to differentiate between modeling the skin effect and proximity effect, a more detailed two-segment structure is developed, with further details shown in Fig. 3(b). Segment "Part A" comprises a four-layer RL-ladder network to represent the skin effect, augmented by an additional resistor to account for the winding's dc behavior. Segment "Part B" models the proximity effect using a three-layer ladder network with mutual inductance coupling between windings of different phases. In order to simplify the model's complexity while maintaining accuracy in representing frequency-dependent phenomena across various ranges, the inductive coupling among the U, V, and W phases is limited to the same branch and the corresponding RL layers.

This two-part ladder network approach (RL + RM) allows for a more accurate representation of high-frequency influences, as it separates the effects of internal eddy current redistribution (skin effect) from external magnetic interactions (proximity effect). While RL ladder networks have been widely adopted in previous studies, the introduction of RM ladder networks for frequency-dependent proximity effect modeling is relatively new. It provides an enhanced level of accuracy for power electronics and electric machine applications.

The capacitive coupling within the machine must also be considered in high-frequency modeling. The parallel circuit highlighted in red in Fig. 3(a), which connects each phase to the machine housing, is designed to represent the frequency-dependent phenomena within the insulation system. On the left, a resistor with a relatively high resistance value models the insulation resistance, while the central capacitor represents the parasitic capacitance between the windings and the housing. In addition, another RC structure is introduced to describe the dielectric loss, which intensifies with increasing frequency. Moreover, the capacitor marked in yellow models the parasitic capacitance within each winding. The dielectric loss along the

Fig. 4. Modeled cable set.

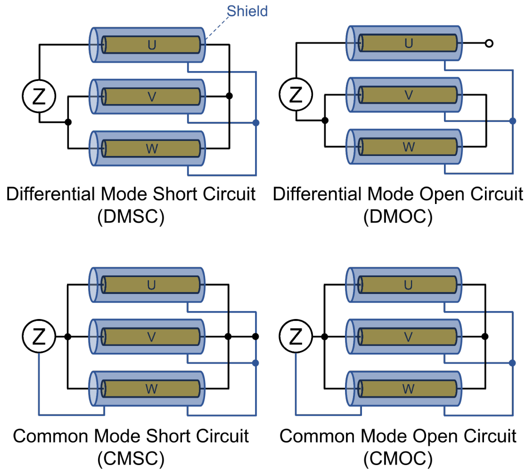

Fig. 5. Measurement topologies for impedance measurement of the three-phase power cables.

winding is neglected due to its negligible magnitude. Finally, for the winding of each phase, an inductance is incorporated to account for the influence of the instrument terminals under high-frequency excitation.

It is important to emphasize that the complexity of this model can be modularly adjusted based on the characteristics of the impedance spectrum obtained from measurements. The applicability of the model is not limited by the type of the studied machine.

B. Development of the Cable Set Model

1) Impedance Measurement: Fig. 4 illustrates the construction of the modeled cable set. Each cable in the U, V, and W phases comprises an independent conductor, an insulation layer, and a shielding layer. To ensure uniformity across the cables, impedance measurements were conducted under four different topologies, as shown in Fig. 5. During the measurements, all cable shields were short-circuited.

Fig. 6 presents the results of the impedance measurements. In the shorted topologies (DMSC and CMSC), the impedance spectra display a noticeable capacitive characteristic within the frequency range below 100 kHz, indicating that the parasitic capacitance between the conductor and the shield cannot be ignored. Above 1 MHz, additional resonance points become evident in the impedance spectra, particularly in common-mode topologies (CMSC and CMOC). This phenomenon, resulting from the electromagnetic interactions among the conductor, insulation layer, and shielding layer within the cable set, must be carefully considered by modeling.

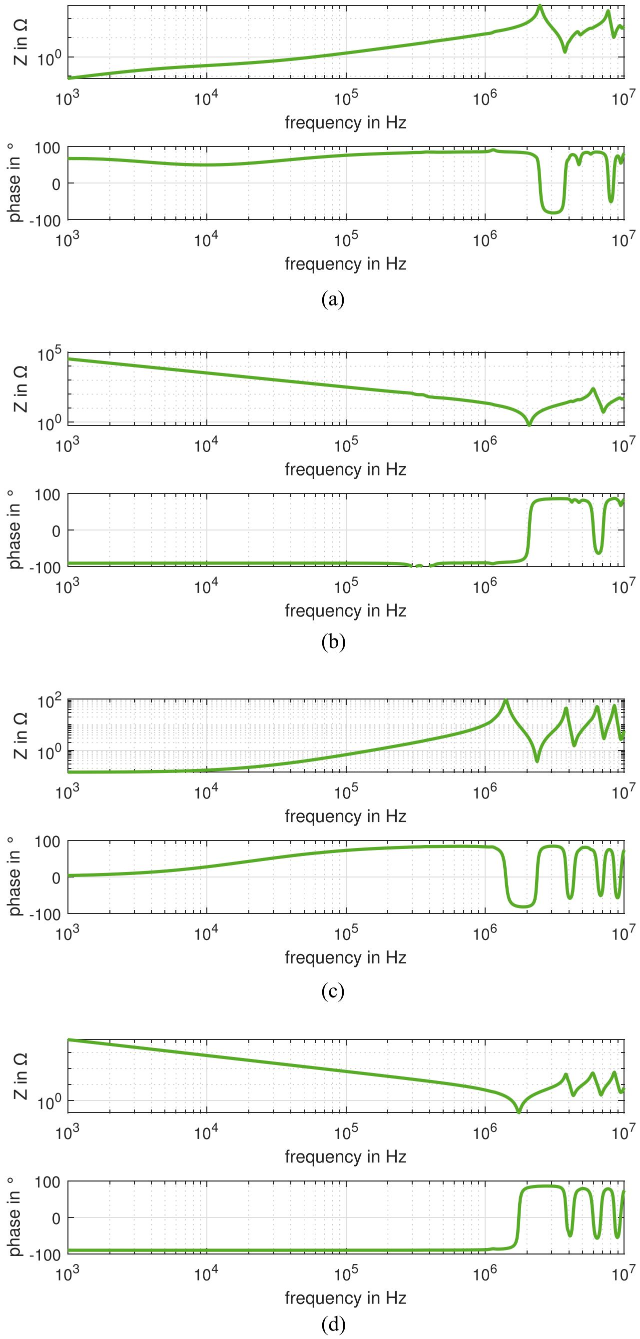

(a)

(b)

(c)

(d)

Fig. 6. Impedance measurement results of the cable set: (a) DMSC, (b) DMOC, (c) CMSC, and (d) CMOC.

2) Grey-Box Model Implementation: Fig. 7 presents the structural overview of the cable model. Since the shielding layers of the cable set are consistently short-circuited during both the impedance measurements and subsequent test bench validations, the modeling process assumes that the wires of all three phases are coupled to a common equivalent shielding layer. Similar to winding modeling, the modular grey-box model with four branches, based on the two-segment structure shown in Fig. 3(b), accounts for both skin and proximity effects. This

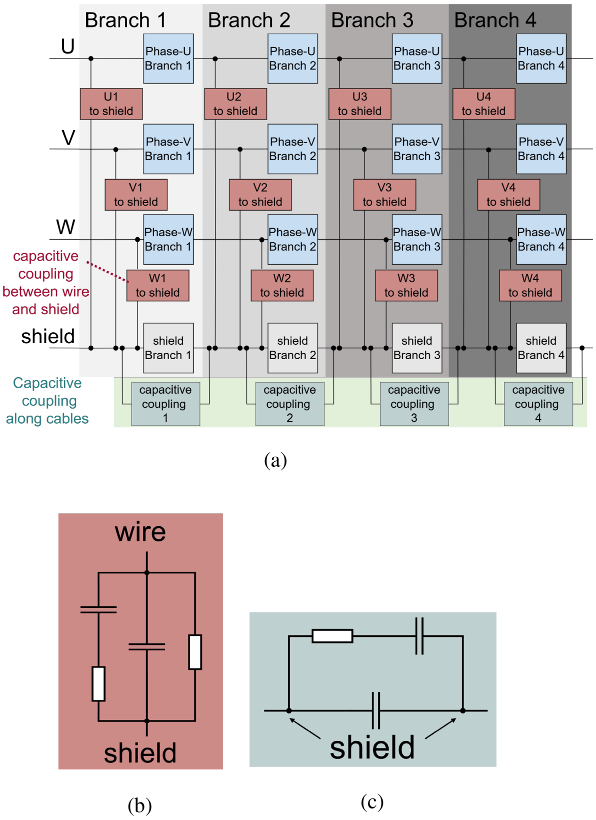

(a)

(b)

(c)

Fig. 7. Grey-box model of the cable set. (a) Structural overview. (b) Model structure of coupling between wires and shield. (c) Model structure of capacitive coupling along shield.

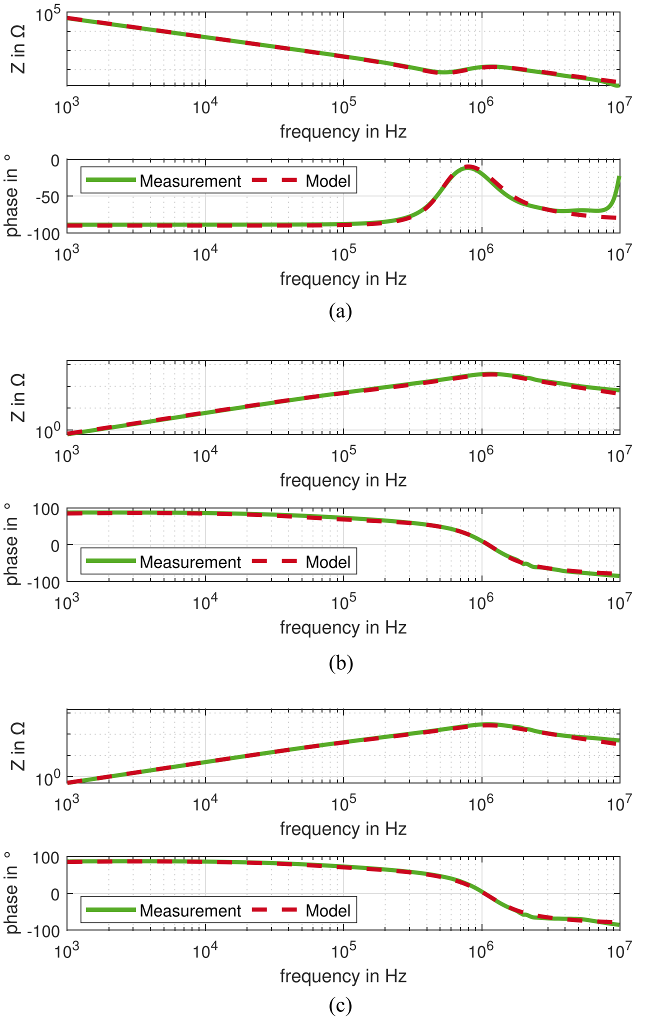

(a)

(b)

(c)

Fig. 8. Examples of modeled and measured impedance spectra of the PMSM stator winding. (a) U-GND. (b) U-V. (c) U-VW.

structure is used to model the three-phase wires (blue blocks) and the shield (grey blocks). The capacitive coupling between the shield and the phase wires is modeled using the same principles as the machine insulation system, incorporating three parallel branches, as shown in Fig. 7(b). A resistor represents the dc properties of the insulation layer, while a capacitor models the corresponding parasitic resistance. In addition, a series RC structure is used to describe the dielectric loss in the vertical direction. Furthermore, the parasitic capacitance and dielectric loss along the cable, primarily caused by the insulation layer materials, are also considered. This effect is integrated into the shield model [green blocks in Fig. 7(a)] through parallel capacitors and an RC structure, as depicted in Fig. 7(c).

C. Model Validation in the Frequency Domain

The model parameterization is achieved using optimization algorithms that minimize the discrepancy between modeled and measured impedance spectra. This study adopts the same parameter identification methods as described in [18]. Figs. 8 and 9 present the measured and modeled impedance spectra for the PMSM and cable set, respectively. The impedance amplitude and phase angle determine the model's frequency response. However, when the model is evaluated, the relative error becomes statistically unreliable because the phase angle crosses zero as the frequency increases. To address this, a normalized index is introduced to evaluate the model's performance in the frequency domain. As described in Sections II-A and II-B, the grey-box model is represented as an equivalent circuit composed of linear passive components, qualifying it as a Linear Time-Invariant (LTI) system. Consequently, for each measurement topology, the modeled impedance spectrum is characterized by the frequency response function (FRF) $G_1(j\cdot\omega)$, where current is the input $I(j\cdot\omega)$ and voltage $U(j\cdot\omega)$ is the output in the frequency domain with $\omega = 2\pi f$ as angular frequency

$$G_1(j\cdot\omega) = \frac{U(j\cdot\omega)}{I(j\cdot\omega)}. \tag{2}$$

$G_1(j\cdot\omega)$ can be transformed into a frequency-based representation $G_1(f)$ as follows:

$$G_1(f) = G_1(j\cdot\omega)\big|_{\omega=2\pi f}. \tag{3}$$

Meanwhile, the measured impedance spectrum serves as the true realization of this FRF, denoted as $G_2(f)$. Both $G_1(f)$ and $G_2(f)$ can be reconstructed from their respective spectra

$$G_1(f_i) = Z_1(f_i)\cdot(\cos\varphi_1(f_i) + j\cdot\sin\varphi_1(f_i)) \tag{4}$$

$$G_2(f_i) = Z_2(f_i)\cdot(\cos\varphi_2(f_i) + j\cdot\sin\varphi_2(f_i)) \tag{5}$$

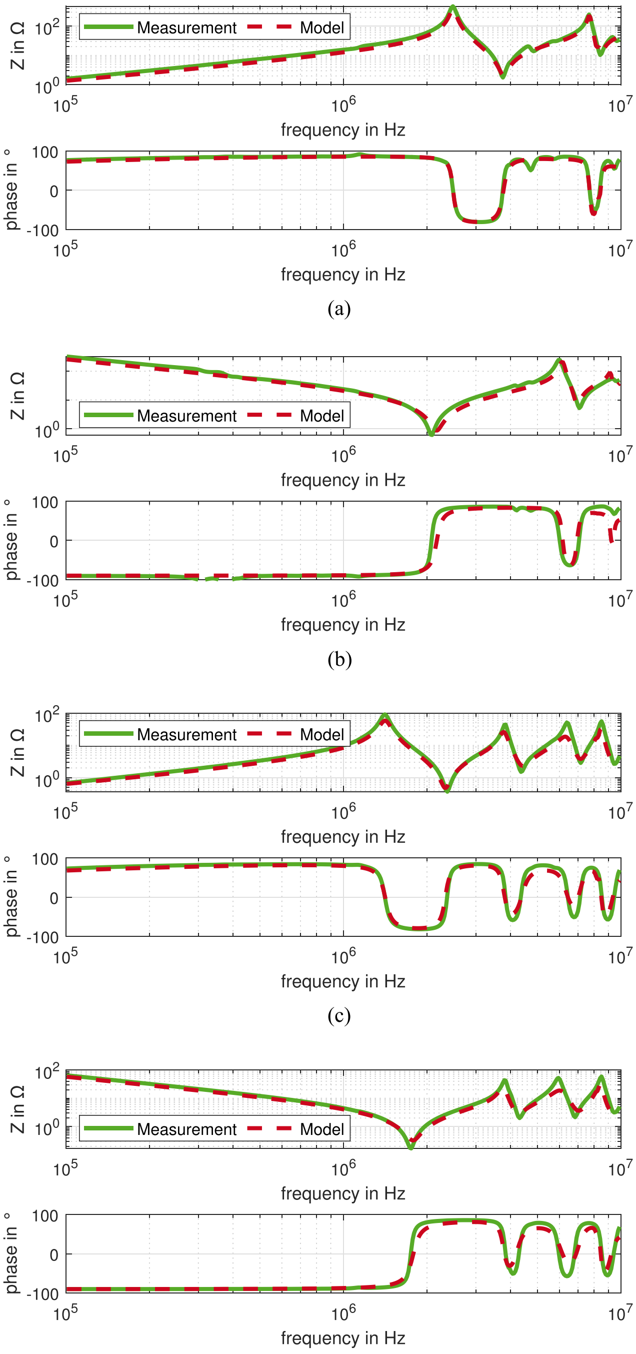

(a) (b) (c) (d)

Fig. 9. Modeled and measured impedance spectra of the cable set. (a) DMSC. (b) DMOC. (c) CMSC. (d) CMOC.

where by

1) Z_1, Z_2: The modeled and measured impedance amplitudes at frequency f_i.
2) φ_1, φ_2: The modeled and measured impedance phase angles at frequency f_i.

In this study, we introduce the magnitude-squared coherence coefficient $C_{G_1G_2}$ [29] to assess the accuracy of the high-frequency model's ability to replicate the frequency-domain characteristics of the windings and cable set

TABLE II
VALIDATION OF GREY-BOX MODEL IN FREQUENCY DOMAIN WITH COHERENCE COEFFICIENT

Model	**Topology**	**Coherence Coefficient with** $f_i \in$ [1 kHz, 10 MHz]	[1 MHz, 10 MHz]
PMSM winding	U-GND	0.99995	0.99793
	V-GND	0.99996	0.99706
	W-GND	0.99995	0.99923
	U-V	0.99840	0.99849
	V-W	0.98850	0.98847
	W-U	0.98944	0.98943
	U-VW	0.99695	0.99700
	V-WU	0.99522	0.99524
	W-UV	0.99226	0.99253
Cable Set	DMSC	0.99313	0.99313
	DMOC	0.99997	0.95090
	CMSC	0.93712	0.93715
	CMOC	0.99999	0.95068

$$C_{G_1G_2} = \frac{|S_{G_1G_2}(f)|^2}{S_{G_1G_1}(f) \cdot S_{G_2G_2}(f)} \in [0, 1]. \tag{6}$$

Here, $S_{G_1G_2}(f)$ represents the cross-power spectral density between $G_1(f)$ and $G_2(f)$, calculated as follows:

$$S_{G_1G_2}(f) = \frac{1}{N}\sum_{i=1}^{N} G_1(f_i) \cdot G_2^*(f_i) \tag{7}$$

where $G_2^*(f_i)$ denotes the complex conjugate of $G_2(f_i)$. Furthermore, the auto-power spectral densities of G_1 and G_2, denoted as $S_{G_1G_1}(f)$ and $S_{G_2G_2}(f)$, respectively, are defined as follows:

$$S_{G_1G_1}(f) = \frac{1}{N}\sum_{i=1}^{N} |G_1(f_i)|^2 \tag{8}$$

$$S_{G_2G_2}(f) = \frac{1}{N}\sum_{i=1}^{N} |G_2(f_i)|^2. \tag{9}$$

The coherence coefficient $C_{G_1G_2}$ reveals the consistency of system responses $G_1(f)$ and $G_2(f)$ under identical input conditions and is used in this article as a metric for evaluating the effectiveness of high-frequency modeling in the frequency domain. Its values range from 0 to 1 as follows:

1) $C_{G_1G_2} = 1$ indicates perfect correlation between the modeled and real system frequency responses, demonstrating an ideal representation in the frequency domain.
2) $C_{G_1G_2} = 0$ indicates that the frequency responses of the model and the real system are completely uncorrelated.

For both grey-box models of cables and machines, the coherence coefficient $C_{G_1G_2}$ was calculated to quantify the agreement between the modeled and measured impedance spectra across the frequency range of 1 kHz to 10 MHz. The results are summarized in Table II . In all topologies, a $C_{G_1G_2}$ higher than 0.93 was achieved. For the PMSM winding model, the average coherence coefficient is 0.9956, while for the cable model, it is 0.9916. Focusing on the critical frequency range above 1 MHz, the $C_{G_1G_2}$ for all topologies remains above 0.93, with an average value of 0.9954 for the machine model and 0.9578 for the cable model. These values, which are very close to 1, indicate that

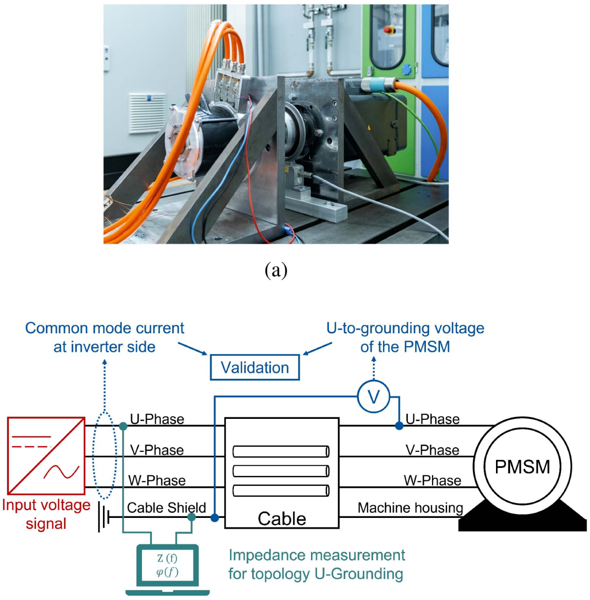

(a)

(b)

Fig. 10. Test bench for time-domain validation. (a) The test bench with an operating PMSM. (b) The measurement setup consists of a SiC power module-integrated inverter, power cables, the PMSM, and associated sensors.

both models can accurately capture the dynamic behavior and characteristics of the modeled subjects in the frequency domain.

III. Influence of Test Bench Environment

A. Impact of Test Bench Configuration on Impedance Spectra

The grey-box models for the machine windings and cables are developed separately. However, these two models need to be integrated based on their setup on the test bench for further validation in the time domain. Fig. 10(b) shows the measurement setup for time-domain validation. Using the 3-phase cable set, the SiC power module-integrated inverter serves as the power source connected to the PMSM. The machine housing and cable shield are grounded. To study the influence of the test bench environment on the components, the impedance between the three-phase terminals on the inverter side and ground is measured with three topologies: U-grounding, V-grounding, and W-grounding. The corresponding impedance spectra, expected to match the measured impedance, are calculated using the integrated models described in Section II for comparison.

Fig. 11 presents an example of the impedance measurement. As observed, the impedance calculated by the integrated model begins to exhibit a noticeable deviation from the measured values on the test bench above 1 MHz, despite the high accuracy of both the PMSM model and the cable model described in Section II.

Fig. 12 illustrates the detailed impedance spectra over this critical frequency range. The corresponding coherence coefficients $C_{G_1G_2}$ are presented in Table III. Compared to the values of both separate models over the same frequency range for all topologies listed in Table II, the $C_{G_1G_2}$ values show a significant decrease. For the U-grounding and V-grounding topologies, the $C_{G_1G_2}$

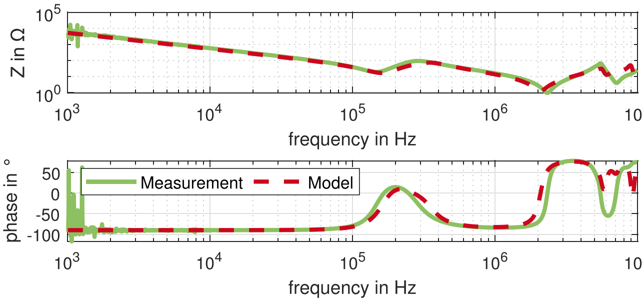

Fig. 11. Modeled and measured impedance for the "V-grounding" topology on the test bench from 1 kHz to 10 MHz.

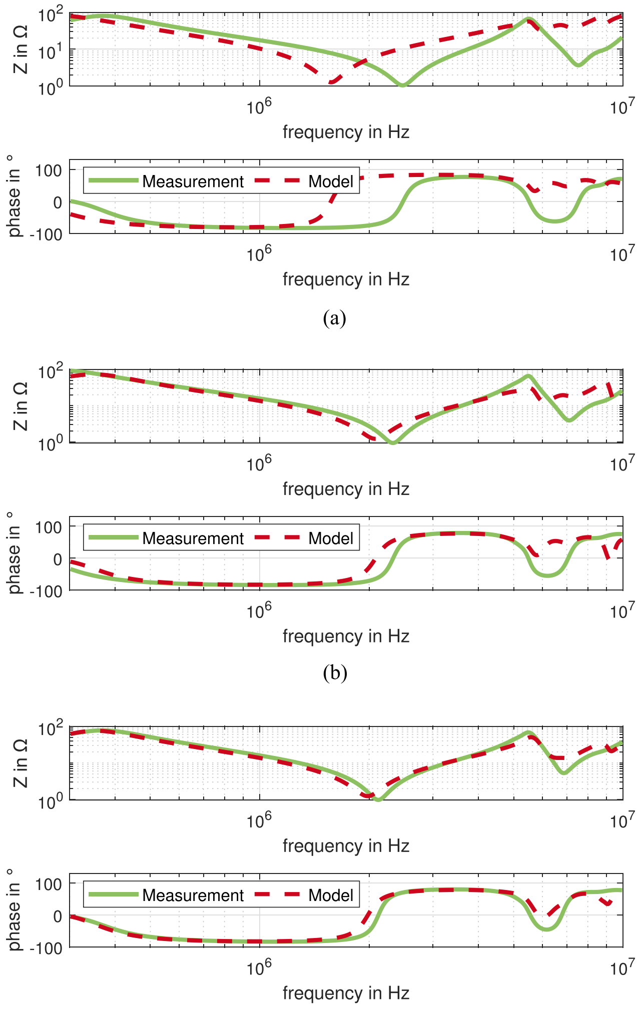

(a)

(b)

(c)

Fig. 12. Modeled and measured impedance on the test bench from 300 kHz to 10 MHz. (a) U-grounding. (b) V-grounding. (c) W-grounding.

TABLE III
THE COHERENCE COEFFICIENT BETWEEN MODELED AND MEASURED IMPEDANCE SPECTRA ON THE TEST BENCH OVER FREQUENCY RANGE FROM 1 MHz TO 10 MHz

Topology	Coherence Coefficient
U-grounding	0.35634
V-grounding	0.49094
W-grounding	0.81387

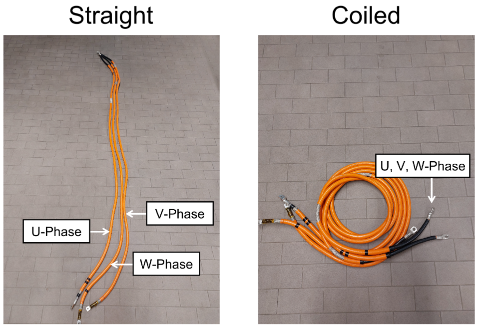

Fig. 13. Cables in various geometrical layouts.

values decreased to 0.356 and 0.491, respectively. These values approach 0, indicating a significant loss of model accuracy in the frequency domain. In other words, modeling the machine winding and cable set independently and then combining them fails to accurately capture the true characteristics of the electrical drive system on the test bench. Further investigation into the underlying causes is required, along with subsequent adjustments to improve the models.

B. *Discussion About Influence of Test Bench Environment*

Both impedance measurements were performed at room temperature with the machine unloaded. Therefore, when analyzing the unexpected discrepancies between the measured and modeled impedance on the test bench, the influences of temperature, humidity, and electromagnetic interference can be excluded.

The stator winding impedance, primarily determined by the machine's geometrical construction and material properties, remains stable over short periods in a relatively stable external environment. Since impedance is measured using weak signals, the insulation system remains unaffected, ensuring the machine model retains high accuracy despite variations in the testing environment.

However, the impedance of the cable is not only influenced by the conductor material, but also by factors such as its structure, layout method, outer sheath, and shielding layer. Changes in the cable's geometry can directly affect its inductance and capacitance distribution, thereby altering its impedance characteristics. In particular, variations in geometry may induce coupling effects between the internal conductors, leading to changes in the cable's mutual impedance. Similarly, alterations in the layout method can impact the electromagnetic properties of the cable, modifying its self-inductance, mutual inductance, and shielding effectiveness, which in turn affect its impedance.

In order to validate this hypothesis, an additional experiment is conducted using another three-phase cable set similar to the one modeled in Section II. Impedance measurements above 100 kHz are performed for the cable set under two different geometrical layouts: a straight layout, consistent with the one in Section II-B for impedance modeling of cables, and a coiled layout, as shown in Fig. 13. The topologies in Fig. 5 are measured.

Table IV lists the coherence coefficients $C_{G_1G_2}$ between the two layouts above 1 MHz, calculated using (7). For the topologies DMSC, CMSC, and CMOC, $C_{G_1G_2}$ drops below 0.5, indicating inconsistent frequency response behavior of the same cable set under different geometrical configurations and winding methods. Notably, for the shorted topologies (DMSC and CMSC), $C_{G_1G_2}$ approaches 0, signifying uncorrelated behavior between the two layouts, as shown in Fig. 14. The three-phase cable setup on the test bench, connected via the machine's neutral point, closely resembles these two topologies. This similarity explains why the geometric configuration and winding method of cables significantly influence the impedance spectral characteristics of the electric drive system above 1 MHz. In addition, the relatively minor variations in $C_{G_1G_2}$ of topology DMOC suggest that the parasitic capacitance between the wire and shield is not the main cause of the impedance spectrum variation in the test bench. This factor will be considered in future model adjustments.

TABLE IV
COHERENCE COEFFICIENT OF THE IMPEDANCE SPECTRA OF AN IDENTICAL CABLE SET BETWEEN STRAIGHT AND COILED LAYOUTS FROM 1 MHz TO 10 MHz

Topology	Coherence Coefficient
DMSC	0.30980
DMOC	0.92221
CMSC	0.16164
CMOC	0.12819

IV. MODEL ADJUSTMENT AND VALIDATION

A. *Frequency-Domain Model Adjustment*

Due to the phenomenon observed in Section III-A, a model adjustment based on the test bench environment is necessary. Section III-B attributes this to changes in the cable set's properties caused by environmental factors. Using the parameterized cable model from Section II, the resistance and inductance values in the RL-ladder "part-A," as well as the dc resistance values describing insulation behavior in the "to Shield" module in Fig. 7(b), remain constant. However, variations in the proximity effect due to the test environment are reflected in changes to the mutual inductance coefficients. These changes in the mutual inductance coefficients apply only in the high-frequency range, specifically to the 2-nd and 3-rd layers of the RL-ladder "Part-B." The remaining capacitive coupling parameters, except the dc-insulation resistance, are also adjusted based on the "to-grounding" impedance measured on the test bench. The PMSM model remains unaltered. The parameter adjustment process is executed using the optimization algorithm mentioned in Section II. For the capacitive coupling parameters, a 10 % variation is allowed based on the parameters of the unadjusted cable model. The cost function described in [18], which describes the similarity degree between measured and modeled impedance spectra, is set as the criterion to halt the search. Fig. 15 shows the model impedance after adjustment, demonstrating clear agreement between the model spectrum and measurements over the critical frequency range above 1 MHz. Table V presents the corresponding $C_{G_1G_2}$ values over this range. For all topologies, values above 0.98 highlight the accuracy of the adjusted model

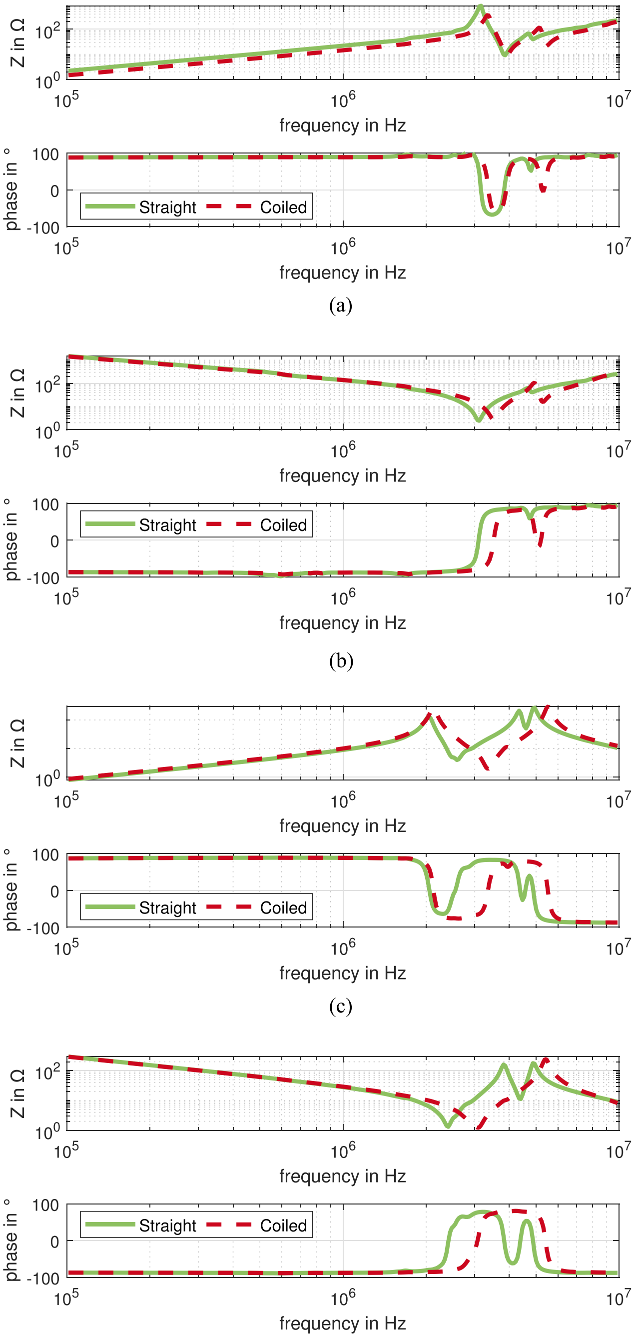

(a)

(b)

(c)

(d)

Fig. 14. Impedance of a cable set under two different layouts: (a) DMSC, (b) DMOC, (c) CMSC, and (d) CMOC.

TABLE V
COHERENCE COEFFICIENT BETWEEN MODELED AND MEASURED IMPEDANCE SPECTRA ON THE TEST BENCH AFTER ADJUSTMENT OVER FREQUENCY RANGE FROM 1 MHz TO 10 MHz

Topology	Coherence Coefficient
U-grounding	0.99560
V-grounding	0.98679
W-grounding	0.99021

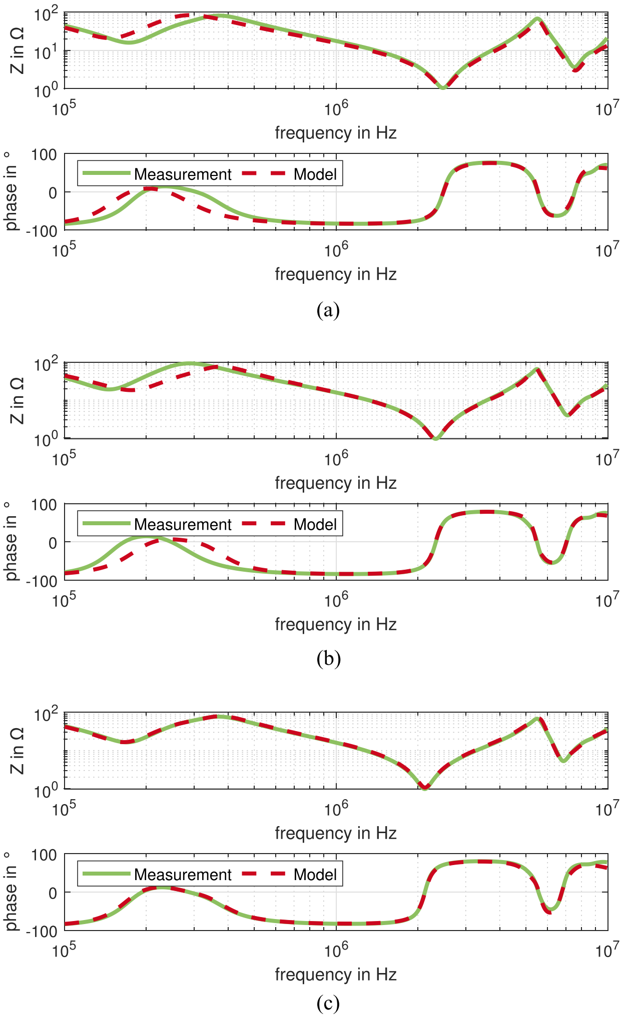

(a)

(b)

(c)

Fig. 15. Modeled impedance on the test bench after adjustment from 300 kHz to 10 MHz. (a) U-grounding. (b) V-grounding. (c) W-grounding.

in reflecting the frequency response behavior of the electrical drive system within this frequency range on the test bench.

B. Validation of the Adjusted Model Using Signals in the Time Domain

The measurement data on the test bench is applied to validate the adjusted integrated model, as illustrated in Fig. 10(b). The PMSM is powered by the SiC-power-module integrated inverter via three-phase cables. The inverter-side common-mode current I_{CM} and the voltage between the PMSM terminal and ground $U_{\text{U-gnd}}$ are selected for comparison with simulated signals. Validation is performed under varying PWM switching frequency f_{SW}, machine rotation speed n_{EM} in a no-load condition.

Figs. 16 and 17 present examples of time-domain validation. The current is measured using a Rogowski current transducer named CWTHF 3B, with a 3dB-bandwidth of up to 15 MHz, while the voltage is measured using a differential voltage transducer named MDP701 from Micsig, with a 3dB-bandwidth of up to 150 MHz. During the measurement of common mode current,

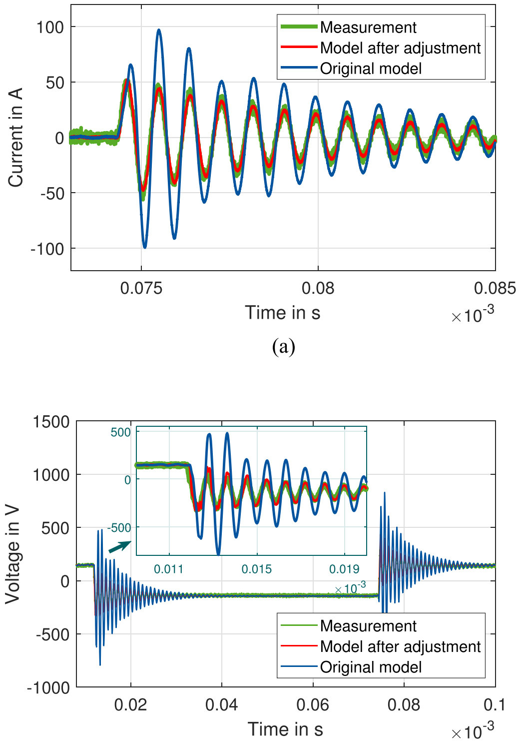

(a)

(b)

Fig. 16. Validation on the test bench under PWM-frequency 8 kHz, rotation speed 0 rpm, load torque 0 Nm: (a) using signal I_{CM}, (b) using signal $U_{\text{U-gnd}}$.

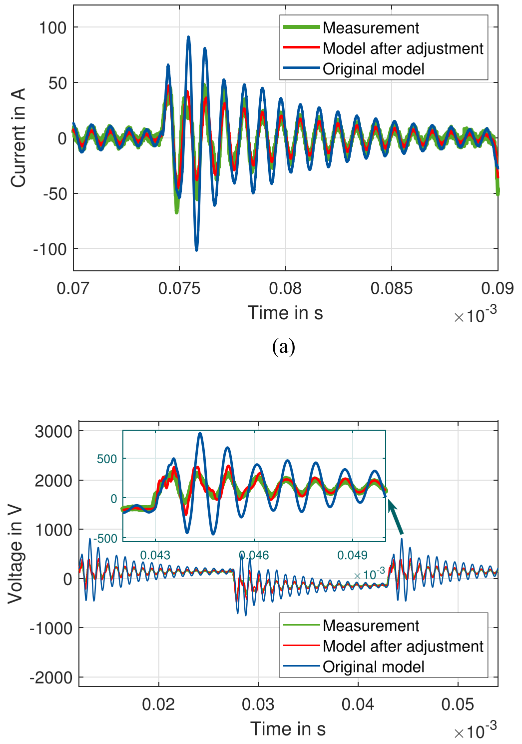

(a)

(b)

Fig. 17. Validation on the test bench under PWM-frequency 32 kHz, rotation speed 100 rpm, load torque 0 Nm: (a) using signal I_{CM}, (b) using signal $U_{\text{U-gnd}}$.

TABLE VI
STATISTICS OF VALIDATION RESULTS ON THE TEST BENCH UNDER DIFFERENT PWM SWITCHING FREQUENCIES AND ROTATION SPEEDS WITH THE ADJUSTED CABLE MODEL CONSIDERING TEST BENCH ENVIRONMENT

		I_{CM}		$U_{\text{U-gnd}}$	
f_{sw} [kHz]	n_{EM} [rpm]	Δ_{peak} [%]	$\Delta_{f_{\mathrm{osc}}}$ [%]	Δ_{peak} [%]	$\Delta_{f_{\mathrm{osc}}}$ [%]
8	0	4.72	4.72	16.44	8.29
	10	6.69	6.69	3.02	4.82
	100	7.46	54.90	4.98	0.72
16	0	9.24	9.24	12.85	0.72
	10	5.30	5.30	3.54	10.49
	100	15.63	15.63	28.11	2.73
32	0	14.59	14.59	6.17	12.89
	10	2.06	2.06	8.50	6.82
	100	15.82	15.82	19.36	20.29

TABLE VII
STATISTICAL ANALYSIS OF SIMULATION RESULTS USING THE UNADJUSTED MODEL

		I_{CM}		$U_{\text{U-gnd}}$	
f_{sw} [kHz]	n_{EM} [r/min]	Δ_{peak} [%]	$\Delta_{f_{\mathrm{osc}}}$ [%]	Δ_{peak} [%]	$\Delta_{f_{\mathrm{osc}}}$ [%]
8	0	80.43	11.12	128.54	11.12
	10	99.67	69.28	115.74	13.93
	100	157.51	14.74	93.55	21.74
16	0	89.79	7.23	136.66	13.14
	10	93.47	9.62	153.03	20.58
	100	108.89	10.72	90.94	19.71
32	0	99.37	8.35	146.02	0.50
	10	91.91	6.45	142.18	11.04
	100	99.84	26.60	155.84	6.22

the Rogowski coil circulates three-phase conductors in the inverter cabinet without including the cables' shields. The overlap between the measured and simulated signals from the adjusted model, for both I_{CM} and $U_{\text{U-gnd}}$, demonstrates the model's ability to accurately capture the transient behavior of the electrical drive system under various switching frequencies and rotation speeds. This outcome aligns with the accurate impedance modeling in the frequency domain, as presented in Fig. 15. In addition, the original integrated model exhibits relatively large discrepancies, indicating that the influence of the test bench environment cannot be neglected during high-frequency modeling. To quantitatively assess the accuracy of the model, the relative errors of the peak value Δ_{peak} and the oscillation natural frequency $\Delta_{f_{\mathrm{osc}}}$ are calculated for both validation signals. Table VI summarizes the results. For I_{CM}, the average relative error in Δ_{peak} is 9.05%, while the average error in $\Delta_{f_{\mathrm{osc}}}$ is 7.69%. Similarly, for $U_{\text{U-gnd}}$, the corresponding values are 16.98% and 8.00%, respectively.

For comparison, the simulation results obtained with the unadjusted model are summarized in Table VII. For I_{CM}, the average relative error in Δ_{peak} is 102.13%, while the average error in $\Delta_{f_{\mathrm{osc}}}$ is 18.23%. Similarly, for $U_{\text{U-gnd}}$, the corresponding errors are 129.16% and 13.11%, respectively.

The validation results demonstrate that adjustments to the high-frequency model based on the test bench environment significantly enhance the model's accuracy. For the inverter-side common-mode current I_{CM}, the accuracy of peak value prediction improves by approximately 93%, while the prediction accuracy for the oscillation frequency increases by 10.6%. Similarly, for the machine terminal-to-ground voltage $U_{\text{U-gnd}}$, the

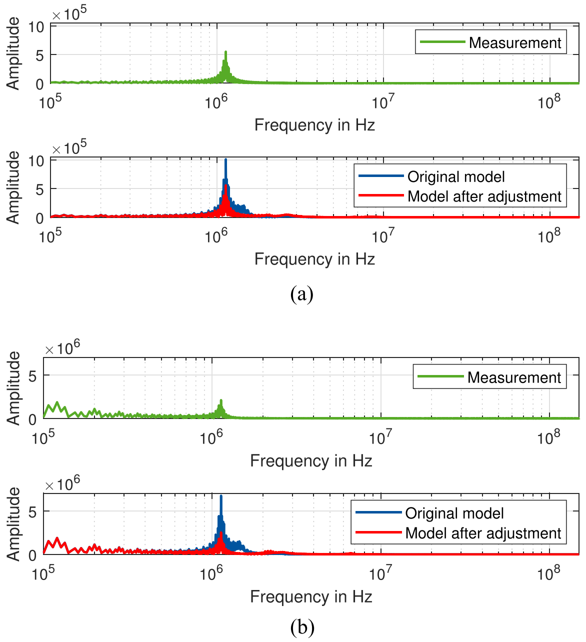

Fig. 18. Validation using spectrum distribution of signals measured on the test bench under PWM-frequency 8 kHz, rotation speed 100 rpm, load torque 0 Nm: (a) using signal I_{CM}, (b) using signal $U_{\text{U-gnd}}$.

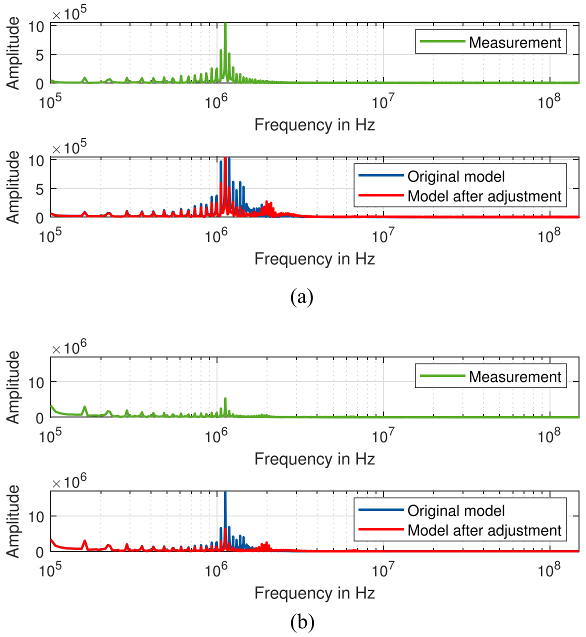

Fig. 19. Validation using spectrum distribution of signals measured on the test bench under PWM-frequency 32 kHz, rotation speed 100 rpm, load torque 0 Nm: (a) using signal I_{CM}, (b) using signal $U_{\text{U-gnd}}$.

prediction accuracy for the peak value and oscillation frequency improves by 111.2% and 5.11%.

Besides the validation results in the time domain, the frequency spectrum of measured and simulated signals is presented in Figs. 18 and 19, whereby Fig. 18 corresponds to the signals in Figs. 16 and 19 corresponds to the voltage signals in Fig. 17. In the frequency domain, the measurement and simulation results using the adjusted model considering test bench influences overlap more than the original model without considering the impact.

These findings emphasize that the influence of the test bench environment on the drive system, particularly the behavior of the cable set, cannot be overlooked during high-frequency modeling. The adjusted model effectively captures the frequency-domain response characteristics of the electric drive system and accurately reflects its transient behavior during the inverter switching process.

V. CONCLUSION

This contribution presents a universal grey-box high-frequency model that incorporates electromagnetic coupling, effectively capturing the frequency-dependent properties and transient behaviors of electric machines and cable sets under various conditions. It underscores the critical importance of accounting for test bench environment influences in high-frequency modeling of electrical drive systems. By addressing geometric and electromagnetic interactions within the test bench setup, the adjusted model achieves high accuracy, validated across both frequency and time domains. The findings highlight that traditional high-frequency modeling approaches, which treat components independently without considering integration effects, can lead to substantial inaccuracies. This research provides a robust foundation for precise high-frequency modeling, facilitating the optimization of insulation systems and enhancing the reliability of electrical drive systems in automotive and industrial applications. Future work will aim to refine the model for broader use cases and explore its potential for real-time monitoring of electrical drives.

REFERENCES

[1] O. E. Özçiflikçi, M. Koç, S. Bahçeci, and S. Emiroğlu, “Overview of pmsm control strategies in electric vehicles: A review,” *Int. J. Dyn. Control*, vol. 12, no. 6, pp. 2093–2107, 2024.

[2] M. Popescu, J. Goss, D. A. Staton, D. Hawkins, Y. C. Chong, and A. Boglietti, “Electrical vehicles—Practical solutions for power traction motor systems,” *IEEE Trans. Ind. Appl.*, vol. 54, no. 3, pp. 2751–2762, May/Jun. 2018.

[3] H. Wang and J. Leng, “Summary on development of permanent magnet synchronous motor,” in *Proc. Chin. Control And Decis. Conf. (CCDC)*. IEEE, 2018, pp. 689–693.

[4] M. Buffolo et al., “Review and outlook on GAN and SiC power devices: Industrial state-of-the-art, applications, and perspectives,” *IEEE Trans. Electron Devices*, vol. 71, no. 3, pp. 1344–1355, Mar. 2024.

[5] M. F. Rahman, P. Niknejad, and M. Barzegaran, “Comparing the performance of Si IGBT and SiC MOSFET switches in modular multilevel converters for medium voltage pmsm speed control,” in *Proc. IEEE Texas Power Energy Conf. (TPEC)*. IEEE, 2018, pp. 1–6.

[6] Y. Zhang, Q. Meng, Y. Wang, D. Lu, and H. Cao, “A coil short-circuit fault diagnosis method based on overvoltage of electromagnetic coil in active magnetic bearing,” *IEEE Trans. Ind. Electron.*, vol. 72, no. 5, pp. 5452–5460, May 2025.

[7] S. Yunus, W. Ming, and C. E. Ugalde-Loo, “Motor overvoltage mitigation using SiC-based zero-voltage switching inverter,” *IEEE Trans. Power Electron.*, vol. 39, no. 1, pp. 1195–1208, Jan. 2023.

[8] Y. Xu et al., “Impact of high switching speed and high switching frequency of wide-bandgap motor drives on electric machines,” *IEEE Access*, vol. 9, pp. 82866–82880, 2021. .

[9] IEC 60034-18-41: *Rotating Electrical Machines - Part 18-41: Functional Evaluation of Insulation Systems - Test Procedures for Voltage Endurance of Insulation Systems, International Electrotechnical Commission (IEC)*, Std. IEC 60034-18-41, 2014.

[10] M. Ghassemi, "Accelerated insulation aging due to fast, repetitive voltages: A review identifying challenges and future research needs," *IEEE Trans. Dielectr. Electr. Insul.*, vol. 26, no. 5, pp. 1558–1568, May 2019.

[11] J. Dittmann, C.-N. Behrendt, and B. Ponick, "Prediction of the voltage distribution in a inverter-fed hairpin stator winding," in *Proc. 25th Int. Conf. Elect. Machines Syst. (ICEMS)*. IEEE, 2022, pp. 1–6.

[12] O. Magdun, S. Blatt, and A. Binder, "Calculation of stator winding parameters to predict the voltage distributions in inverter fed ac machines," in *Proc. 9th IEEE Int. Symp. Diagnostics Electric Machines, Power Electron. Drives (SDEMPED)*. IEEE, 2013, pp. 447–453.

[13] R. L. Stoll, *The Analysis of Eddy Currents*. Clarendoon Press, pp. 4–6, 1974.

[14] B. H. Lin, J. T. Tsai, and K. L. Lian, "A non-invasive method for estimating circuit and control parameters of voltage source converters," *IEEE Trans. Circuits Syst. I: Reg. Papers*, vol. 66, no. 12, pp. 4911–4921, Dec. 2019.

[15] V. Karakaşli, F. Gross, T. Braun, H. De Gersem, and G. Griepentrog, "High-frequency modeling of delta-and star-connected induction motors," *IEEE Trans. Electromagn. Compat.*, vol. 64, no. 5, pp. 1533–1544, May 2022.

[16] S. Sundeep, J. Wang, and A. Griffo, "Holistic modeling of high-frequency behavior of inverter-fed machine winding, considering mutual couplings in time domain," *IEEE Trans. Ind. Appl.*, vol. 57, no. 6, pp. 6044–6057,Jun. 2021.

[17] H. Peng et al., "Voltage distribution modeling along stator windings in permanent magnet synchronous machines using coil-based grey box models," *IEEE Trans. Energy Convers.*, vol. 39, no. 3, pp. 1994–2007, Sep. 2024.

[18] H. Peng, Y. Yu, and K. Hameyer, "Conductor-based modeling of a single-tooth winding for emi simulation," *IEEE Trans. Power Electron.*, vol. 39, no. 9, pp. 11099–11109, Sep. 2024.

[19] H. Peng and K. Hameyer, "A method of deriving an equivalent permeability spectrum of ferrous materials considering all effects in electrical machines for 2-D magneto-dynamic simulations," *IEEE Trans. Ind. Electron.*, vol. 71, no. 12, pp. 16245–16254, Dec. 2024.

[20] H. Peng, Z. Luo, Y. Yu, and K. Hameyer, "Modeling voltage distribution along the hairpin windings of an electrical machine using impedance fitting," in *Proc. Int. Conf. Elect. Machines (ICEM)*. IEEE, 2024, pp. 1–7.

[21] H. Peng et al., "High-frequency modeling of permanent magnet synchronous machines using grey box models," *IEEE Trans. Transport. Electrific.*, vol. 10, no. 4, pp. 8150–8160, Apr. 2024.

[22] H. Peng, Y. Yu, S. Stevic, S. Mönninghoff, and K. Hameyer, "Coil-based high-frequency modeling of permanent magnet synchronous machines with single-tooth windings," *Arch. Elect. Eng.*, pp. 151–163, 2025.

[23] M. Rahman, T. Haider, E. Haque, T. Blackburn, and C. Grantham, "Modelling and experimental studies of effects of steep fronted inverter waveforms on motor and supply cabling and their remedies," in *Proc. IEEE Int. Conf. Power Electron. Drive Systems. PEDS'99 (Cat. No 99TH8475)*, vol. 1. IEEE, 1999, pp. 519–524.

[24] P. Yi, P. K. S. Murthy, and L. Wei, "Performance evaluation of SiC MOSFETS with long power cable and induction motor," in *Proc. IEEE Energy Convers. Congr. Expo.*.IEEE, 2016, pp. 1–7.

[25] I. Stevanović, B. Wunsch, G. L. Madonna, and S. Skibin, "High-frequency behavioral multiconductor cable modeling for emi simulations in power electronics," *IEEE Trans. Ind. Informat.*, vol. 10, no. 2, pp. 1392–1400, Feb. 2014.

[26] Y. Wu, K. Choksi, M. ul Hassan, and F. Luo, "An extendable and accurate high-frequency modelling of three-phase cable for prediction of reflected wave phenomenon," in *Proc. IEEE Appl. Power Electron. Conf. Expo.*(APEC).IEEE, 2022, pp. 944–950.

[27] A. Hoffmann and B. Ponick, "Method for the prediction of the potential distribution in electrical machine windings under pulse voltage stress," *IEEE Trans. Energy Convers.*, vol. 36, no. 2, pp. 1180–1187, Feb. 2020.

[28] H. Peng et al., "A study about the influence of rotor position of ipmsm on the maximum voltage on motor terminals under inverter-fed operation," in *Proc. IEEE 6th Student Conf. Electric Machines Syst.*. IEEE, 2023, pp. 1–6.

[29] J. S. Bendat and A. G. Piersol, *Random Data: Analysis and Measurement Procedures*. Hoboken, NJ, USA: Wiley, 2011.

Hujun Peng received the bachelor's degree in electrical engineering from Zhejiang University, Hangzhou, China, in June 2013, and the master's degree in electrical engineering from Dresden University of Technology, Dresden, Germany, in October 2017, and the Ph.D. degree in electrical engineering from RWTH Aachen University, Aachen, Germany, in 2023.

Since February 2023, he has been working as a Postdoctoral Researcher with the Institute of Electrical Machines. His research interests include high-frequency modeling of electrical machines and characterization of insulation systems in machines.

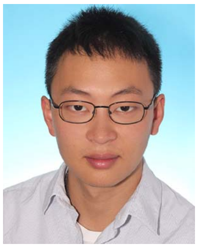

Yue Yu received the master's degree in automation engineering with a specialization in mechatronics from RWTH Aachen University, Aachen, Germany, in November 2023.

Since February 2025, he has been working as a Research Assistant and the Ph.D. student with the Institute of Electrical Machines, RWTH Aachen University. His research interests include high-frequency modeling and design of electrical machines.

Svetomir Stevic (Graduate Student Member, IEEE) received the Diploma in electrical engineering from the School of Electrical Engineering, University of Belgrade, Serbia, in 2011, and the M.Sc. degree in electrical engineering from RWTH Aachen University, Aachen, Germany, in 2016.

From 2016 until 2018, he worked with the Idaho National Laboratory, USA, on power converters. From 2018 to 2024, he worked with the Institute of Electrical Machines, RWTH Aachen University, on topics including co-design and prototyping of electric drives. Since 2024, he has been working with Schabmüller GmbH for electric drives.

Simon Steentjes received the Diploma and Dr.-Ing. degrees in electrical engineering and information technology from RWTH Aachen University, Aachen, Germany, in 2011 and 2017, respectively.

From 2011 to 2018, he served as a Research Associate and Group Leader with the Institute of Electrical Machines (IEM). After completing his Doctorate, He joined Audi AG as a subject matter expert in electric traction machines for xEVs. He then advanced to Group Manager with Hilti Entwicklungsgesellschaft mbH, overseeing the Electric Motor Development Group. Most recently, he served as Group Manager for Electrical Machine and Drive Technology, directing the development of electric drives while spearheading advancements in multi-physical design and integrating innovative control algorithms and position-sensing technologies. In October 2024, he was appointed as a Full Professor with the Chair of Electrical Machines and Drives and Director of IEM at RWTH Aachen University. His research focuses on modeling magnetic and winding materials, with interests in computational electromagnetics, multiphysical, multiscale simulation, sensorless control, and inverter–machine interactions.